ACS OMEGA

http://pubs.acs.org/journal/acsodf

Article

Super-Resolution Residual U-Net Model for the Reconstruction of Limited-Data Tunable Diode Laser Absorption Tomography

Shaogang Chen, Xiaojian Hao,* Baowu Pan, and Xiaodong Huang

Cite This: *ACS Omega* 2022, 7, 18722−18731

Read Online

ACCESS | Metrics & More | Article Recommendations

ABSTRACT: Resolution is an important index for evaluating the reconstruction performance of temperature distributions in a combustion environment, and a higher resolution is necessary to obtain more precise combustion diagnoses. Tunable diode laser absorption tomography (TDLAT) has proven to be a powerful combustion diagnosis method for efficient detection. However, restricted by the line-of-sight (LOS) measurement, the reconstruction resolution of TDLAT was dependent on the size of the detection data, which made it difficult to obtain sufficient data for extreme environmental measurements. This severely limits the development of TDLAT in combustion diagnosis. To overcome this limitation, we proposed a super-resolution reconstruction method based on the super-resolution residual U-Net (SRResUNet) to improve the reconstruction resolution using a software method that could take full advantage of residual networks and U-Net to extract the deep features from the limited data of TDLAT to reconstruct the temperature distribution efficiently. A simulation study was conducted to investigate how the parameters would affect the performance of the super-resolution model and to optimize the reconstruction. The results show that our SRResUNet model can effectively improve the accuracy of reconstruction with super-resolution, with good antinoise performance, with the errors of 2-, 4-, and 8-times super-resolution reconstructions of approximately 5.3, 7.4, and 9.7%, respectively. The successful demonstration of SRResUNet in this work indicates the possible applications of other deep learning methods, such as enhanced super-resolution generative adversarial networks (ESRGANs) for limited-data TDLAT.

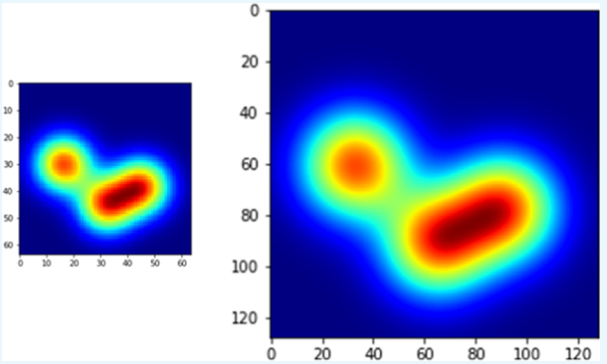

1. INTRODUCTION

The real distributions of temperature and concentration fields in the combustion environment are powerful instruments for combustion diagnosis, reflecting the combustion uniformity and evolution law, which is necessary for an optimized design for high-efficiency and low-carbon-emission gas turbines.[1] Resolution is a significant index for evaluating the richness of detailed information contained in the optical detection system, mainly regarding the spatial and temporal resolution, and reflects the performance of the imaging system in demonstrating object details. For instance, a higher resolution temperature field distribution, with a larger pixel density and richer texture details, will help researchers more precisely analyze the combustion condition and realize a combustion diagnosis with higher reliability.

Tunable diode laser absorption tomography (TDLAT), based on absorption spectroscopy and computerized tomography (CT), is one of the most powerful tools for high-speed combustion flow diagnostics, owing to its noninvasive nature, quick response, and high sensitivity.[2−5] Thus, it is generally adapted to all complex and bad test combustion environments. On the other hand, TDLAT can realize the simultaneous measurement of temperature and gas concentration,[6] which has made it the most popular and necessary technique for research on combustion diagnosis. However, TDLAT is based on the line-of-sight (LOS) detection method, and the reconstruction spatial resolution is mainly dependent on laser numbers through the region of interest (ROI).[7] In practical engineering processes, restricted by the extremely complex test environment, which has made it difficult to arrange enough acquisition equipment, there is a lack of sufficient effective detection data to reconstruct the original distribution, and this has become the key factor limiting the development of TDLAT.[8]

The most direct way to improve the reconstruction resolution is to improve the optical hardware system, such as by optimizing the arrangement of lasers and detectors to acquire more detection data. In previous studies, researchers

Received: March 9, 2022
Accepted: May 12, 2022
Published: May 23, 2022

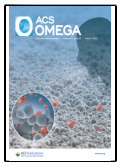

devoted considerable effort to generating a high-resolution reconstruction of the temperature or gas concentration in the combustion environment. The reconstruction system of Doo-Won Choi et al. obtained data from the optical signals of 8-laser beams passed on a cross section of the methane flame.[9] Xia et al. took advantage of two-step tomographic reconstructions and realized an 11 × 11 resolution reconstruction with half the number of detectors.[10] Xu, Liu et al. used a pentagon TDLAS detection system and CT-TDLAS to realize the two-dimensional (2D) temperature and H_2O concentration reconstruction of swirl combustion.[11−14] Choi et al. used multiangle temperature detection equipment that divides the combustion field into 22 × 22 square mesh grids.[15] Jeon et al. constructed a CT-TDLAS system with 16-path cells to measure the two-dimensional temperature distribution of a propane−air premixed flame, covering several fuel mixing conditions.[16] Unfortunately, it is usually difficult to arrange enough hardware to meet high-resolution reconstruction requirements for the detection of an extreme combustion environment. Hardware improvement is limited and the cost is extremely high, becoming a burning problem that demands prompt solutions for researchers.

The residual network (ResNet) is a useful super-resolution method based on a machine learning algorithm with excellent results and extensive applications, such as single image super-resolution.[17,18] The team of White Chang has introduced a deep multiscale residual network in infrared aerothermal nonuniform correction.[19] U-Net is one of the typical prevalent examples of deep learning models and has found extensive applications.[20] For example, a fully dense U-Net has been used for 2-D sparse photoacoustic tomography artifact removal, and Zang et al. combined cascaded Dense-UNet with residual nets to optimize the image super-resolution.[21,22] However, to the best of our knowledge, the combination of both has not been applied to super-resolution reconstruction for TDLAT.

Therefore, from the perspective of soft measurement, we propose an optimized deep learning model to realize super-resolution reconstruction for limited-data TDLAT to compensate for the low reconstruction resolution and inefficiency of existing tomographic algorithms. In this study, combining the advantages of ResNet and U-Net, we designed a super-resolution residual U-Net (SRResUNet) model that has a strong feature extraction ability and can build a map between the detection data and temperature distribution, providing a novel method and supply for high-resolution TDLAT.

The remainder of this work is organized as follows: Section 2 explains the theories and advantages of TDLAT, ResNet, and U-Net; Sections 3 and 4 present the simulation studies including the parameter tuning and the structure design of SRResUNet and the results of the simulation; and finally, the final section concludes this work and proposes future research directions.

2. MATHEMATICAL BACKGROUND

2.1. Tunable Diode Laser Absorption Tomography. Tunable diode laser absorption tomography (TDLAT) is a popular absorption spectroscopy technique[12] that features quick response and high selectivity. Beer's law describes the relationship among temperature T, gas concentration X, pressure P, and absorbance $\alpha(\nu)$. It can be defined as

$$A = \int_{-\infty}^{+\infty} -\ln\left(\frac{I_t(\nu)}{I_o(\nu)}\right)\mathrm{d}\nu = PXS(T)(\varphi(\nu, T))L = \alpha(\nu)L \tag{1}$$

where $I_t(\nu)$ and $I_o(\nu)$ are the intensities of the transmitter laser and the incident laser, respectively; P [atm] is the total pressure of the region of interest; X is the concentration of the material under test; $S[T(x)]$ [cm^{-2} atm^{-1}] is the line strength of the molecular transition of the absorbing species, which is dependent on the temperature;[13,14] $\varphi(\nu,T)$ [cm] is the line-shape function, and $\int_{-\infty}^{+\infty}\varphi(\nu,T)\mathrm{d}\nu \equiv 1$; and L[m] is the length of the absorption path. To reconstruct the original absorbance distribution, a series of absorbance arrays should be obtained by repeating (1) and discretizing as $A_{\nu_n,i}$ for the LOS measurements, organized as follows

$$A_{\nu_n,i} = \sum_{j=1}^{J}[PS(\nu_n, T)X]_i L_{i,j} = \sum_{j=1}^{J}\alpha_j L_{i,j} \quad (i = 1, 2, 3\cdots I) \tag{2}$$

where j represents the jth pixel, J is the total number of pixels within the discretized field, $L_{i,j}$ is the absorption path length of the ith beam within the jth pixel, and the total number of beams is L, as shown in Figure 1. To simplify the calculation, it

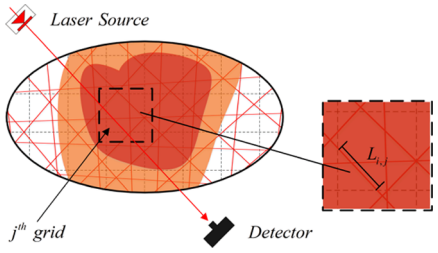

Figure 1. Schematic diagram of the Beer−Lambert law.

can often be substituted into eq 3 and matrix form 4, where L is the matrix of the length of the absorption path and α_{ν_n}. is the matrix of absorbance of laser ν_n [cm^{-1}].

$$\begin{cases} A_{\nu_i,1} = \alpha_{\nu_i,1}L_{1,1} + \alpha_{\nu_i,2}L_{1,2} + \cdots + \alpha_{\nu_i,J}L_{1,J} \\ A_{\nu_i,2} = \alpha_{\nu_i,1}L_{2,1} + \alpha_{\nu_i,2}L_{2,2} + \cdots + \alpha_{\nu_i,J}L_{2,J} \\ \cdots \\ \cdots \\ A_{\nu_i,I} = \alpha_{\nu_i,2}L_{I,1} + \alpha_{\nu_i,2}L_{I,2} + \cdots + \alpha_{\nu_i,J}L_{I,J} \end{cases} \tag{3}$$

$$A_{\nu_n,i} = L\cdot\alpha_{\nu_n} \tag{4}$$

2.2. Residual Networks. Compared with traditional neural networks, a deep learning method with a deeper network can extract more abstract and abundant features.[23] However, an increase in the number of networks will cause a saturation or even a decrease in the accuracy rate on the training set, called the problems of degenerate, mainly because the structure of the deep network is more complex and the gradient descent algorithm is more likely to obtain local optimal solutions. This problem has a negative effect on the application of deep learning networks.

To overcome this problem, residual networks (ResNet) were designed to retain the depth of deep networks and take advantage of shallow networks to avoid degenerate problems. As shown in Figure 2, the most important characteristic of

https://doi.org/10.1021/acsomega.2c01435
ACS Omega 2022, 7, 18722−18731

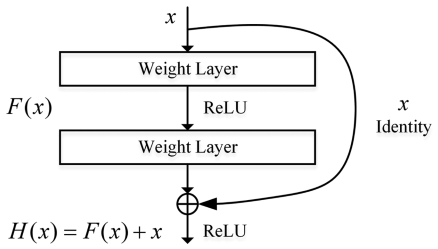

Figure 2. Schematic diagram of residual blocks.

ResNet is identity mapping, which skips the interlayer and is introduced to the final output, whereas the other part is called residual mapping, sharing the same function as the normal feedforward neural network.

This connection method is called a shortcut connection,[18] and the learning object becomes the residual, which can be defined as

$$F(x) = H(x) - x \tag{5}$$

where $F(x)$ and $H(x)$ are the maps before and after summation, respectively. In this way, the original input can play a more important role in reflecting the output, retaining the important information and reducing the loss for the whole network just needing to learn the difference between the input and the output with a simplified learning objection and lower training difficulty.

2.3. Super-Resolution Reconstruction with U-Net. U-Net is a typical deep convolutional neural network (DCNN) featuring local receptive fields, feature map fusion, and lightweight features.[20] The distribution structure of the combustion field is always simple and fixed, which means that too many complex models, such as most SOTA algorithms always based on large parallel corpora,[24] would reduce the risk of overfitting. However, unlike a full convolutional neural network (FCN), the most unique feature is the structure of the skip connection and splice of feature maps. As shown in Figure 3, the middle connection between downsampling and upsampling can introduce low-level extractions of the networks to the final process, which reduces the loss of useful features.

In the study of the reconstruction field, the difficulties are mainly related to the recovery of the high-frequency signal, referring to the place of intensity changing drastically, mainly because of the loss of edge information in each space. Apparently, U-Net takes advantage of the splice of feature maps with skip connections and can effectively extract the deep abstract information (high-level features) and retain the structural information (low-level features), adapting to few-feature extraction in the reconstruction combustion environment.

As depicted in Figure 3, the key processes of U-Net generally include convolution, downsampling (pooling), upsampling, and skip connection processes. The typical downsampling method is max pooling, which is used to reduce the resolution of images and obtain abstract and high-level features, caring more about the semantic information of images. The typical upsampling method is deconvolution, which can also be described as the backward propagation of normal forward propagation without updating the gradient. In the field of super-resolution reconstruction, the function of U-Net can be described as the prediction and generation of a new high-resolution image from original low-resolution images. Hence, the loss function of U-Net usually uses L2 loss and is defined as

$$\text{loss}_{\text{reconsturction}} = \frac{1}{n}\sum_{k=1}^{K}(y_k - f(x_i))^2 \tag{6}$$

where K is the total number of pixels, and y_k and $f(x_i)$ are the true and predicted values of the kth pixel, respectively.

By repeating the training and validating the model until the loss function converges, the parameters of the model structure can be determined and used to reconstruct the 2D field distribution.

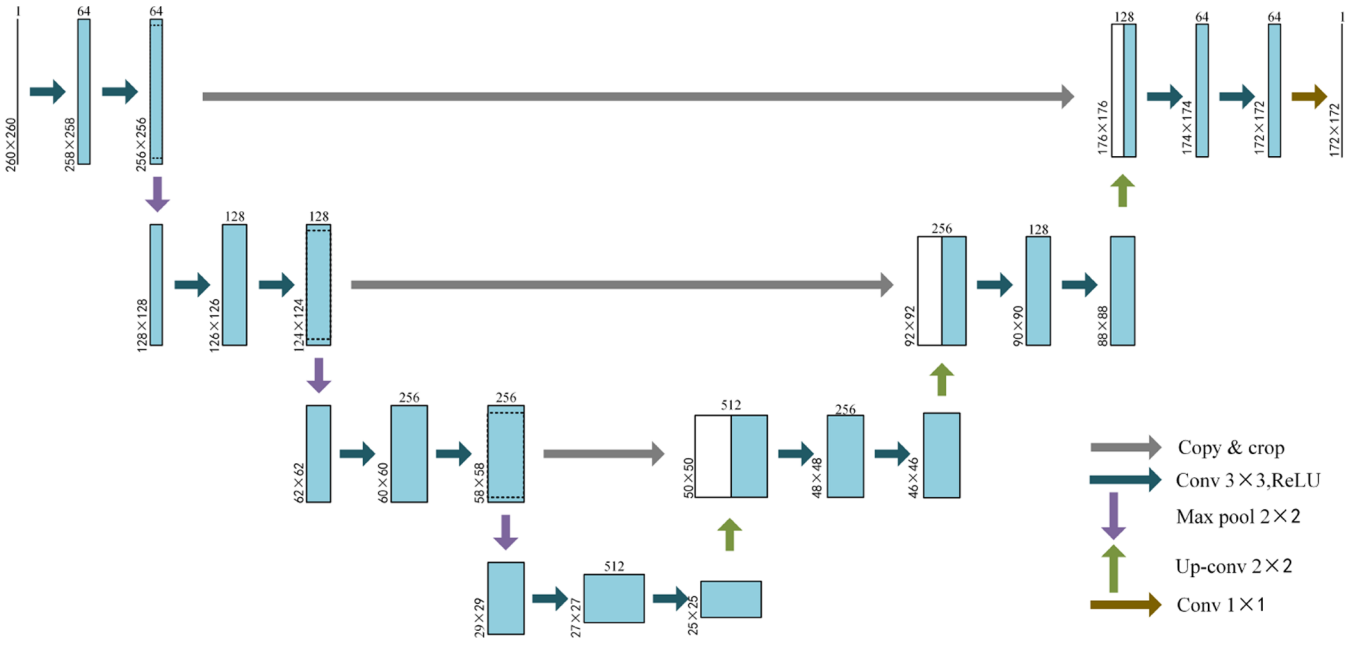

Figure 3. Typical structure of U-Net.

https://doi.org/10.1021/acsomega.2c01435
ACS Omega 2022, 7, 18722−18731

3. SETTINGS FOR SIMULATIVE STUDIES

In this section, simulation studies have been conducted to verify the feasibility of SRResUNet for super-resolution reconstruction problems of limited-data TDLAT, mainly regarding the preparation of the data set, the design of the network, and the standard of quality assessments.

3.1. Preparation of Data Set. TDLAT is an LOS detection method, and the reconstruction quality is based on the number of laser paths, consisting of detecting angles and channels.[13] In preliminary research, we found that more detection angles could improve the imaging quality of TDLAT, as shown in Figure 4. In particular, the resolution of the

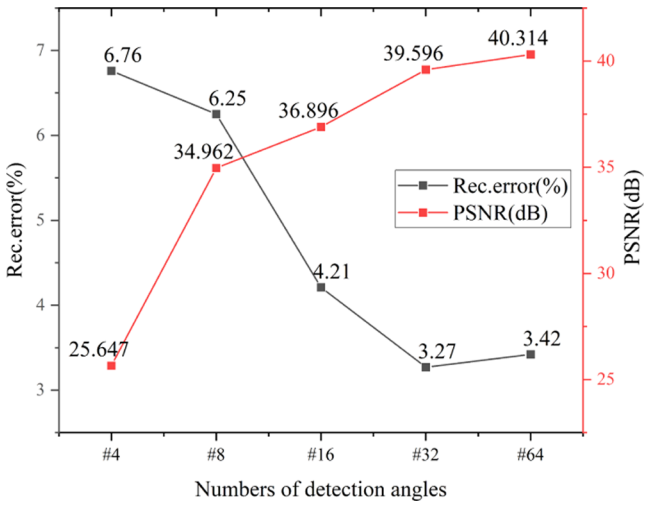

Figure 4. Effects of different numbers of detection angles on the reconstruction quality.

reconstructed image was dependent on the number of channels for each angle. Hence, to realize super-resolution with limited data, limited angles and channels were considered.

Primarily, 20,000 samples were artificially created: 12,000 for training, 4000 for validation, and 4000 for testing. Each sample contained a high-resolution (HR) temperature distribution T_{HR} (128 × 128) and low-resolution absorbance A_{data}. To simulate the limited detectors and projection angle detection in practice, different small quantity projection angles and channels were simulated, including 8, 16, and 32 angles with 16, 32, and 64 channels. Hence, we obtained $A_{8\times16}(8 \times 16)$, $A_{16\times32}(16 \times 32)$, and $A_{32\times64}(32 \times 64)$ LR absorbance arrays based on eq (4).[25] To meet the requirements of complex multimodal flames encountered in practical combustion environments, the temperature distribution was generated with one to three randomly distributed Gaussian peaks on top of a flat plane, simulating the typical combustion temperature from 1000 to 2500 K, as shown in Figure 5. T_{HR} was set as the label for identification and A_{data} was set as the input data for the network.

3.2. Design of the Network. Because the process and method of reconstructing both distributions were similar,[26] we illustrated how this SRResUNet model was designed for temperature super-resolution reconstruction based on TDLAT in this work. With the aim of comparing different magnification-time super-resolution reconstruction performances, the amplification of SRResUNet was set as 8, 4, and 2. The amplification times N_A were determined by the number of symmetric layers N_l, and the relationship is defined as

$$N_A = 2^{N_l - 1} \tag{7}$$

Considering $N_A = 4$ as an example, the overall design of the SRResUNet architecture is shown in Figure 6a. The input size was 2# (16 × 32) on behalf of the two absorbance arrays with 16 angles and 32 channels for each angle. To meet the reconstruction of the (128 × 128) distribution, 4-times super-resolution and $N_l = 3$ were required. We set up the first layer with two 32# (3 × 3) convolution kernels at the beginning to extract shallow features. The convolution kernel numbers of the second and third layers were 64# (3 × 3) and 128# (3 × 3), respectively, with a stride size of 1 and maintaining the size of the feature mapping. The residual and amplification networks, including the residual blocks and pixel-padding network, are shown in Figure 6b. The former was used to extract hidden features, and the latter was used to create more pixels and map the features. Copy and amplification connections were set up to fuse the original and abstract high-level features. The average pooling operations were all performed with (2 × 2) filters, called downsampling, as shown in Figure 6c. The overall design of convolution kernels is referred to as $N_k = 32 + 64 + 128$. After the U-shaped symmetric residual network for feature extraction is designed, the map of the characteristics can be converted into a vector of

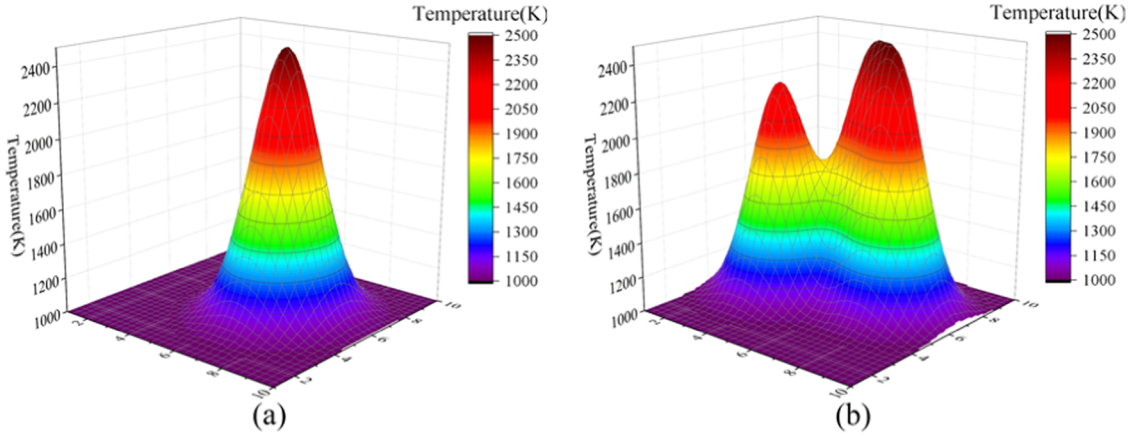

Figure 5. Simulated distribution of temperature. (a) Temperature distribution example with a randomly distributed Gaussian peak; (b) temperature distribution example with two randomly distributed Gaussian peaks for the simulation studies.

https://doi.org/10.1021/acsomega.2c01435
ACS Omega 2022, 7, 18722−18731

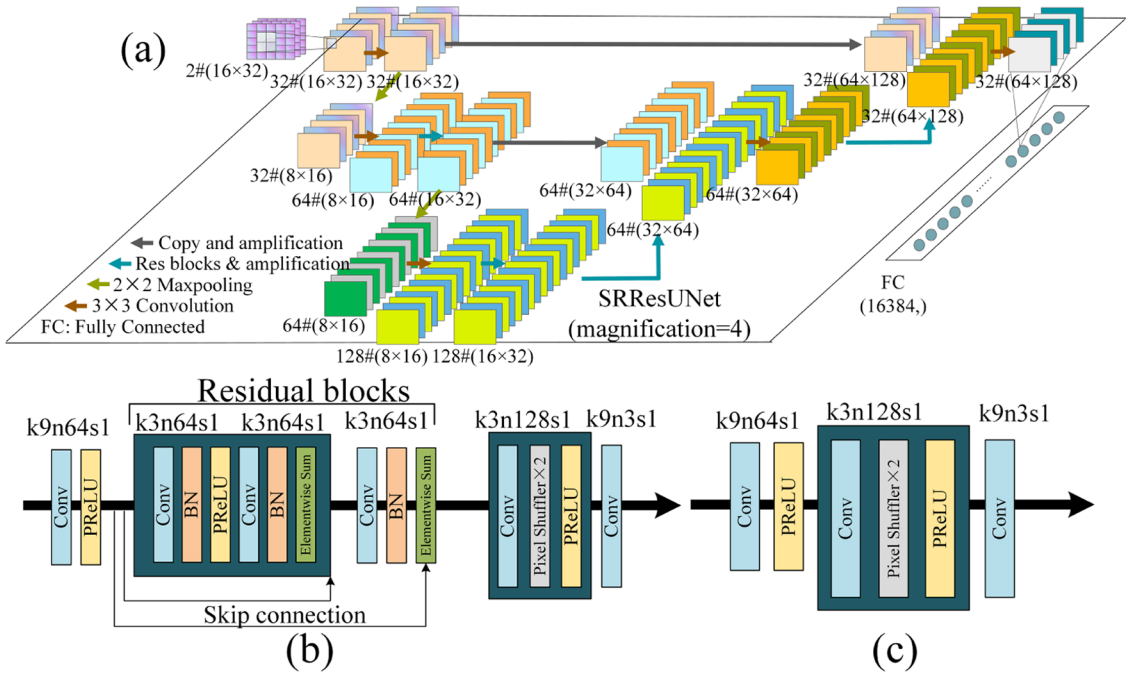

Figure 6. (a) Design of the SRResUNet architecture (magnification time = 4); (b) one of the designs of residual blocks and amplification; and (c) one of the designs of copy and amplification.

temperature distribution (16384), which can be easily reformed as a (128 × 128) temperature distribution as the expected HR output.

In particular, the SRResUNet structure designed in this work has the following characteristics:

(a) Easy to transplant and expand: the structure of each layer was extremely similar and the amplification times, which meant that we could realize different magnifications of super-resolution reconstruction by simply cropping one model.

(b) Dynamic learning rate adjustment: the exponential decay mode was used to update the learning rate with a fast convergence.

$$l_r(n) = l_r(0)\cdot e^{-n/g},\ g = 10000 \tag{8}$$

where $l_r(0)$ and $l_r(n)$ are the learning rates in the 0th and nth epochs, respectively; and g is the global step designed.

A parametric rectified linear Uni (PReLU) was introduced as the activation function. This method considers both positive and negative responses and effectively extracts low-level features, avoiding the loss of low-level features in the combustion temperature distribution.

$$\mathrm{PReLU}(x) = \begin{cases} x, & \text{if } x \geq 0 \\ \alpha\cdot x, & \text{if } x < 0 \end{cases} \tag{9}$$

The loss function of this design was defined in eq 6, and the adaptive moment estimation (Adam) optimization method was chosen as the optimizer, which was based on the momentum and RMSProp methods,[27] combining the advantages of inertia retention and situational awareness. Compared with other adaptive learning rate algorithms, the Adam method has a faster convergence speed and more effective learning effect, which can correct the problems existing in other optimization technologies, such as slow convergence of learning rate disappearance or large fluctuation of loss function caused by high-variance parameter updates.

$$\hat{m}_t = \frac{m_t}{1-\beta_1^t} = \frac{\beta_1 m_{t-1} + (1-\beta_1)g_t}{1-\beta_1^t} \tag{10}$$

$$\hat{v}_t = \frac{v_t}{1-\beta_1^t} = \frac{\beta_2 v_{t-1} + (1-\beta_2)g_t^2}{1-\beta_1^t} \tag{11}$$

where β_1 and β_2 are the exponential decay rates, controlling the current gradient and the square of the gradient, which were set as $\beta_1 = 0.9$ and $\beta_2 = 0.99$, respectively; $\hat{m}_t$ and $\hat{v}_t$ are the mean and variance of the time, respectively; and g_t is the first derivative of the objective function of t. The final optimizer can be defined as

$$\theta_t = \theta_{t-1} - \alpha\cdot\frac{\hat{m}_t}{\sqrt{\hat{v}_t} + \varepsilon} \tag{12}$$

where α is the learning rate, and $\varepsilon = 10^{-8}$ is used to avoid dividing 0.

A trained deep learning model, such as SRResUNet, can be considered as a black box. By extracting the features from the TDLAT detecting data and building a map between the LOS data and 2D field distribution, we can quickly generate the reconstruction distribution with satisfactory accuracy.

3.3. Indexes of the Quality Assessment. To quantify the reconstruction performance of SRResUNet, we defined three indices to estimate the errors between the reconstruction distribution and origin distribution, including the peak signal-to-noise ratio (PSNR) and the reconstruction error of the temperature distribution or concentration (Err). These indices are defined as follows

https://doi.org/10.1021/acsomega.2c01435
ACS Omega 2022, 7, 18722−18731

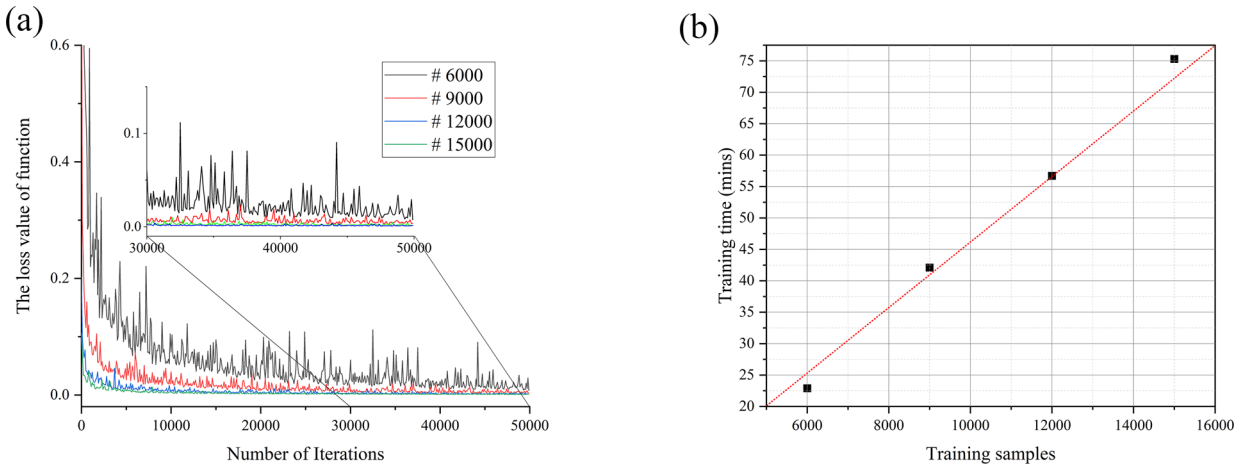

Figure 7. Determination of the number of training samples. (a) Relationship between training samples and the training loss; (b) time cost of training samples.

$$\mathrm{PSNR} = 10\cdot\log_{10}\left(\frac{\mathrm{MAX}_I^2}{\mathrm{MSE}}\right) = 20\cdot\log_{10}\left(\frac{255}{\sqrt{\mathrm{MSE}}}\right)$$

$$\mathrm{MSE} = \frac{1}{mn}\sum_{i=0}^{m-1}\sum_{j=0}^{n-1}[I(i,j) - K(i,j)]^2 \quad (13)$$

where m and n are the height and width of the images; $I(i,j)$ and $K(i,j)$ represent each pixel in the reconstructed and original images.

$$\mathrm{err} = \frac{\Delta}{L}\times 100\% = \frac{\sum_{k=1}^{128\times128}|y_k^* - y_k|}{\sum_{k=1}^{128\times128} y_k^*}\times 100\% \quad (14)$$

where Δ is the absolute error; L is the true value; and y_k^* and y_k are the true value and generated value of the kth pixel of the 128×128 distribution, respectively.

4. RESULTS AND DISCUSSIONS

The super-resolution reconstruction accuracy of the SRResU-Net deep learning model is largely dependent on parameters such as the learning rate l_r, design of the convolution kernels K, number of training samples N_S, and number of amplification times N_A. Hence, the major focus of this section is to investigate how these parameters affect the performance of SRResUNet and how they should be determined. The optimized SRResUNet structure was then used for comparison with the traditional super-resolution imaging method (interpolation, sparse representation) and the deep learning super-resolution method (SRCNN) for the inversion and super-resolution reconstruction of TDLAT problems.

All algorithms were implemented on the same computer with an AMD Ryzen 9 5950X CPU, GeForce RTX 3090-24GB GPU, based on the Windows 10 Professional Edition operating system, Python37, and Pytorch19 environments.

4.1. Effects of Number of Training Samples. Deep learning methods such as DCNN and GANs are data-driven learning models, and it is important to utilize a sufficient number of samples to extract meaningful features during the training and learning process. To explore the effects of the number of training samples on the super-resolution reconstruction accuracy of the temperature distribution, four different sizes of training data sets were generated in the same way, as described above. The parameters were fixed as follows: $l_r = 30e^{-5}$, $K = 32 + 64 + 128$, and $N_A = 4$. The effects of loss and training time are shown in Figure 7. As shown in Figure 7a, the loss fluctuated relatively and exhibited a lower speed of convergence when the number of samples was less than 12,000. However, when the number of samples was more than 12,000, the final losses were very close. Combined with the time cost in Figure 7b, there was a linear correlation between the training time and sample numbers, and it was unwise to adopt too many samples. Hence, 20,000 (12,000 training samples, 3000 validation samples, and 3000 test samples) samples were adopted for the training procedure of SRResUNet.

4.2. Determination of Network Layers and Kernel Design. The design of network layers and kernels is an important factor that determines the feature extraction and model complexity. More kernel channels were used to improve the performance of feature extraction and increase the accuracy of model generation, which increased the time cost and training complexity. Furthermore, deeper layers indicate that more abstract features can be extracted. Through these further characteristics, we realized reconstruction with higher amplification times.

The relationship between the training time and loss value of the different designs of the layers and kernels is shown in Figure 8. Layers 2, 3, and 4 with different kernel designs were simulated to study the convergent behavior of the loss and time cost of the training, with the aim of determining the proper construction of layers and convolution kernels, facilitating a quicker and more effective feature extraction and training process.

As shown in Figure 8, the red line indicates the balance between the time cost and optimal average loss. When $N_A = 4$, $N_l = 3$ was used, SRResUNet convolution channels designed with $K = 32 + 64 + 128$ performed best during the training process, with a related better loss value and faster convergence rate, with $K = 64 + 128$ and $K = 16 + 32 + 64 + 128$. In general, SRResUNet with a few kernels was unable to extract sufficient features from the training data to make a prediction. However, the increase in the number of kernels not only increased the time cost of the training process but also had the risk of overfitting, which was a disaster for model training and testing. For example, the training time for the case $K = 64 +$

https://doi.org/10.1021/acsomega.2c01435
ACS Omega 2022, 7, 18722−18731

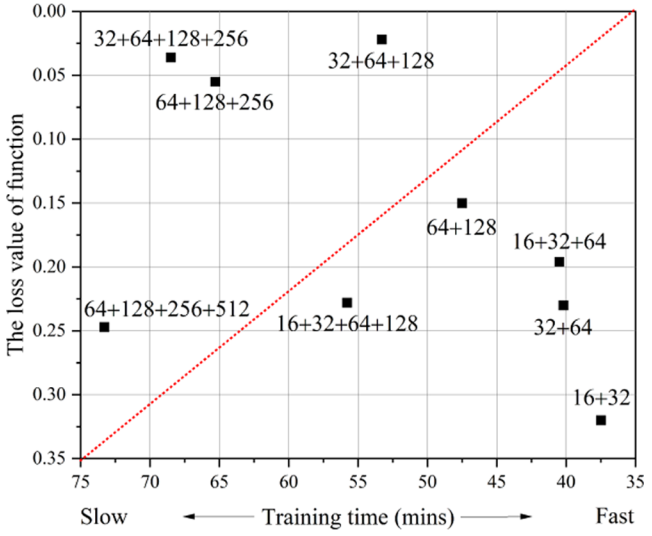

Figure 8. Effects of the design of layers and kernels on the training time and loss function.

128 + 256 + 512 had a quite bad result of the loss. Consequently, considering both the time cost and speed of convergence, the SRResUNet layers and convolution kernels designed were $N_l = 2$, $K = 64 + 128$; $N_l = 3$, $K = 32 + 64 + 128$; and $N_l = 4$, $K = 16 + 32 + 64 + 128$ for the 2-; 4-; and 8-times super-resolution temperature distribution reconstructions, respectively.

4.3. Determination of Learning Rate. The learning rate is a crucial hyperparameter that affects the model training. An ideal learning rate was expected to have a fast speed of convergence and low loss, showing an excellent prediction performance. In contrast, an improper setting would lead to the failure of the training process because of vanishing or exploding gradient problems. The determination of the learning rate was a slightly mathematically rigorous method. However, according to the evolution of the loss function, a proper learning rate can be determined, which is the commonly adopted method in deep learning training.

Keeping the other three parameters the same ($N_S = 20000$, $N_l = 3$, $K = 32 + 64 + 128$), six different types of learning rates were used to train SRResUNet, and the evolution of the respective loss functions is shown in Figure 9. Apparently, when the learning rate was too small (e.g., $l_r = 20e^{-5}$), the loss function converged slowly and could not get to a minimum in a long iteration. With the increase in the learning rate, the convergence was sped up and reconstruction performances were improved. However, when the learning rate was too large, the loss function would produce an abnormal spike (e.g., $l_r = 3e^{-3}$) or be unable to converge (e.g., $l_r = 8e^{-3}$), meaning the failure of the network training. Therefore, for the super-resolution reconstruction studied here, $l_r = 28e^{-5}$ was suggested.

4.4. Experimental Verification and Comparison. Knowing the influence of the number of training samples N_S, the number of network layers N_l, the design of convolution kernel K, and the learning rate l_r on the SRResUNet super-resolution reconstruction accuracy, an effective and high accuracy SRResUNet model to reconstruct the temperature distribution was designed, with $N_s = 15000$, $l_r = 28e^{-5}$; $N_l = 2$, $K = 64 + 128$; $N_l = 3$,$K = 32 + 64 + 128$; $N_l = 4$,$K = 16 + 32 + 64 + 128$ for the 2-; 4-; and 8-times super-resolution reconstructions, respectively. The results based on our designed SRResUNet model of 2-, 4-, and 8-times super-resolution reconstructions are shown in Figure 10. Qualitatively, the three reconstructed distributions shared a high degree of similarity with the original distribution, regardless of the locations or the magnitudes of the peaks. The results demonstrated that the designed SRResUNet effectively extracted the temperature distribution models from the training samples while retaining the smoothness property perfectly in 2- and 4-times super-resolutions.

We have also used the generated SRResUNet model for the reconstruction of some different distributions, such as annular distributions and multimodal distributions, and the results showed that the reconstruction errors of the 4-times super-resolution were all less than 5%, meaning that this super-resolution reconstruction method could be widely adapted to a variety of distributions. The results showed that the reconstruction errors increased with the number of super-resolutions, but were still less than 10% when the 8-times super-resolution reconstruction was performed eight times. As shown in Figure 10, when the super-resolution increased, the reconstruction error was larger. On the other hand, the errors of the highest temperature peak, which had a dramatic change and was called the high-frequency information, were larger than the place of gentle changes. This may be due to the

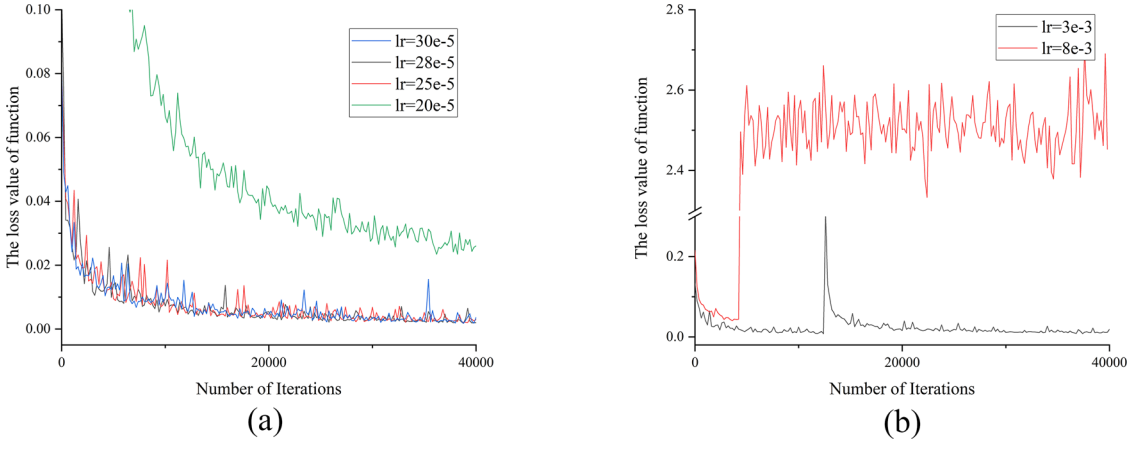

Figure 9. Evolution of the loss function for the six kinds of learning rates. (a) Too small learning rate and some relatively suitable learning rates; (b) too high learning rates.

https://doi.org/10.1021/acsomega.2c01435
ACS Omega 2022, 7, 18722−18731

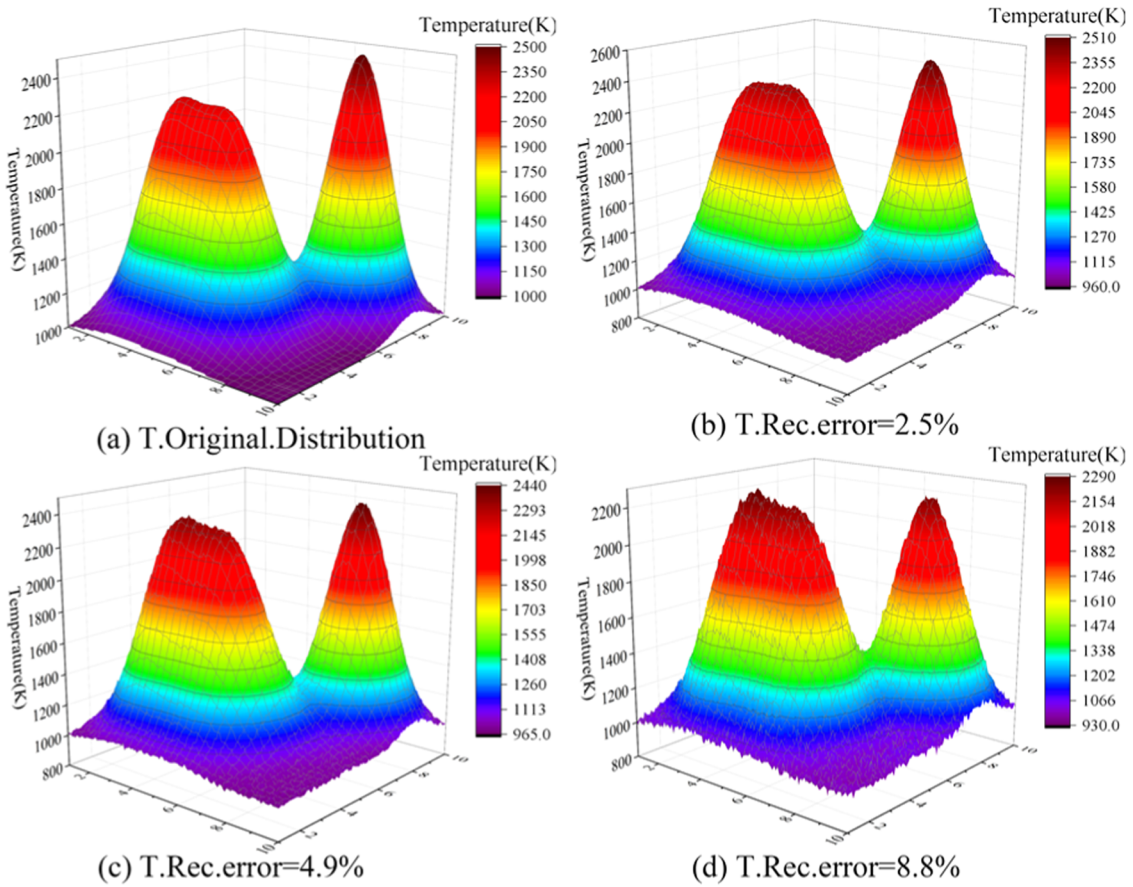

Figure 10. Reconstructed distribution and errors of 2-, 4-, and 8-times super-resolution reconstructions. (a) Original temperature distribution; (b) 2-times reconstruction result; (c) 4-times reconstruction result; and (d) 8-times reconstruction result.

limited amount of LOS measurement data and the inherent lack of spatial resolution, which could not extract enough features to realize excellent reconstruction.

In addition, the detection of the combustion environment is always affected by noise interference. The antijamming capability of the model plays an important role in the super-resolution reconstruction. We added different levels of impulse noise, from 0 to 30%, to the original data to verify the antijamming ability. As shown in Figure 11, the 2-times super-resolution reconstruction had a great antijamming ability and low fluctuation with reconstruction errors of less than 10%. The errors of the 4-times reconstruction were less than 10 when the noise level was less than 25%. In contrast, the antijamming ability and reconstruction errors had comparatively high fluctuations.

To verify the super-resolution reconstruction performance of our SRResUNet in real applications, combustion temperature field testing was conducted. The temperature data were obtained by the TDLAT system consisting of a 760 nm DFB laser diode and a 64-element Si photodiode array (HAMAMATSU) and verified by Infrared Camera ImageIR 5300, whose resolution was 320 × 256.

In this study, the measured combustion field was generated through an explosive fireball simulator with three flamethrowers, and the temperature was around about 2200 K, as shown in Figure 12. The resolution of the obtained temperature field was 8 × 8, and the 2-, 4-, and 8-times super-resolutions were 16 × 16, 32 × 32, and 64 × 64, respectively. To validate the accuracy of the temperature

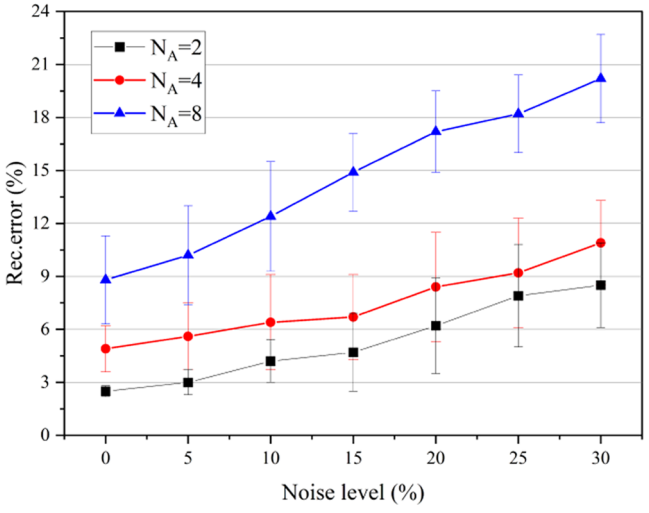

Figure 11. Reconstructed errors of 2-, 4-, and 8-times super-resolution reconstructions under different noise levels.

distribution, the images of ImageIR with 320 × 256 resolution were resized and pooled into the size of 16 × 16, 32 × 32, and 64 × 64. The super-resolution reconstruction performances of the traditional super-resolution method interpolation, sparse representation based on the GA reconstruction method, and machine learning method SRCNN(FCN)[28−30] were compared with our SRResUNet.

https://doi.org/10.1021/acsomega.2c01435
ACS Omega 2022, 7, 18722−18731

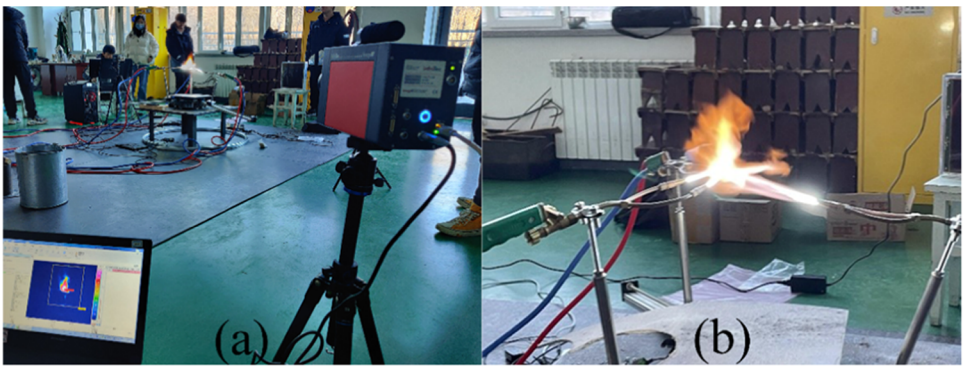

Figure 12. (a) Layout of the experiment site; (b) explosive fireball simulator with three flamethrowers.

The original reconstruction errors of the traditional method were significantly larger than those of SR-FCN and our designed SRResUNet. In other words, the deep learning model has a better super-resolution reconstruction, suggesting a good prospect of deep learning for practical applications. As the super-resolution reconstruction level increased, the reconstruction performance of SR-FCN dropped sharply, the PSNR was only 30.02 dB in the 8-times super-resolution reconstruction, and the reconstruction error was 19.6%. In contrast, SRResUNet had a higher PSNR score and lower reconstruction errors, even with an error of the 8-times reconstruction of less than 10%, as shown in Table 1.

Table 1. Super-Resolution Reconstruction Performances of Different Algorithms

class		PSNR	rec. error (%)
interpolation	×2	26.53	17.1
	×4	19.21	19.2
	×8	16.19	30.1
sparse representation	×2	30.32	16.2
	×4	25.31	21.4
	×8	22.35	26.5
SR-FCN	×2	38.11	8.9
	×4	33.23	16.2
	×8	30.02	19.6
SRResUNet	×2	41.22	5.3
	×4	39.22	7.4
	×8	34.65	9.7

In addition, compared to other algorithms, SRResUNet has an overwhelming advantage in terms of computational efficiency. For the same testing cases, SRResUNet completed each reconstruction in approximately a millisecond class, whereas GA took approximately hours. The critical advantage of SRResUNet is that it is a promising technique for real-time measurements. It should be noted that although the training process of SRResUNet took approximately 5−7 h, once the networks were established, it could be used continuously to process the data.

5. CONCLUSIONS

In conclusion, we developed a novel inversion method for solving super-resolution reconstruction with limited-data TDLAT problems using SRResUNet. The simulation studies performed in this work have shown that the temperature distribution can be rapidly and efficiently reconstructed using our optimized SRResUNet structure with a high antijamming capability, even if the data were limited. Compared with other algorithms, SRResUNet in this study can achieve higher accuracy with a low time cost. The successful implementation also indicates the possible applications of other sophisticated super-resolution models, such as very deep super-resolution convolutional networks (VDSR)[31] and enhanced super-resolution generative adversarial networks (ESRGAN),[32] to TDLAT temperature field super-resolution reconstruction.

AUTHOR INFORMATION

Corresponding Author

Xiaojian Hao − *Science and Technology on Electronic Test and Measurement Laboratory, North University of China, Taiyuan 030051, China; School of Instrument and Electronics, North University of China, Taiyuan 030051, China*; Email: nuc6hxj@163.com

Authors

Shaogang Chen − *Science and Technology on Electronic Test and Measurement Laboratory, North University of China, Taiyuan 030051, China; School of Instrument and Electronics, North University of China, Taiyuan 030051, China*; orcid.org/0000-0002-8147-7411

Baowu Pan − *School of Materials Science and Engineering, North University of China, Taiyuan 030051, China*

Xiaodong Huang − *Science and Technology on Electronic Test and Measurement Laboratory, North University of China, Taiyuan 030051, China; School of Instrument and Electronics, North University of China, Taiyuan 030051, China*

Complete contact information is available at: https://pubs.acs.org/10.1021/acsomega.2c01435

Notes

The authors declare no competing financial interest.

ACKNOWLEDGMENTS

This work was supported in part by the National Natural Science Foundation of China (NSFC) under Grant 52075504; the Fund for Shanxi 1331 Project Key Subject Construction; the Graduate Innovation Project of Shanxi Province (No. 2021Y613); and the Guangdong Provincial Key Laboratory for Electronic Functional Materials and Devices (No. EFMD2020001Z).

REFERENCES

(1) Xiaowen, D.; Li, X.; Hong, Y.; Feng, T.; Qun, Z. Numerical Investigation of Fuel Distribution Effect on Flow and Temperature

https://doi.org/10.1021/acsomega.2c01435
ACS Omega 2022, 7, 18722−18731

Field in a Heavy Duty Gas Turbine Combustor. *Int. J. Turbo Jet-Engines* **2018**, *35*, 71−80.
(2) Nadir, Z.; Brown, M. S.; Comer, M. L.; Bouman, C. A. A Model-Based Iterative Reconstruction Approach to Tunable Diode Laser Absorption Tomography. *IEEE Trans. Comput. Imaging* **2017**, *3*, 876−890.
(3) Krishna, Y.; O'Byrne, S. Tunable Diode Laser Absorption Spectroscopy as a Flow Diagnostic Tool: A Review. *J. Indian Inst. Sci.* **2016**, *96*, 17−28.
(4) Sentko, M. M.; Schulz, S.; Stelzner, B.; Anderlohr, C.; et al. Determination of temperature and water-concentration in fuel-rich oxy-fuel methane flames applying TDLAS. *Combust. Flame* **2020**, *214*, 336−345.
(5) Zhenzhen, W.; Zhou, W. Application of 2D temperature measurement to a coal-fired furnace using CT-TDLAS. *Meas. Sci. Technol.* **2019**, *31*, No. 035203.
(6) Zhang, G.; Wang, G.; Huang, Y.; et al. Reconstruction and simulation of temperature and CO2 concentration in an axisymmetric flame based on TDLAS. *Optik.* **2018**, *170*, 166−177.
(7) Cho, G. R.; Choi, D.-W. Measurement enhancement of TDLAS based on variable weighted cross-correlation tomography for the simultaneous reconstruction of 2D temperature and concentration. *J. Mech. Sci. Technol.* **2021**, *35*, 525−534.
(8) Jeon, M.-G.; Deguchi, Y.; Kamimoto, T.; Doh, D.-H.; Cho, G.-R. Performances of new reconstruction algorithms for CT-TDLAS (computer tomography-tunable diode laser absorption spectroscopy). *Appl. Therm. Eng.* **2017**, *115*, 1148−1160.
(9) Cho, G. R.; Choi, D. W. Measurement enhancement of TDLAS based on variable weighted cross-correlation tomography for the simultaneous reconstruction of 2D temperature and concentration. *J. Mech. Sci. Technol.* **2021**, *35*, 525−534.
(10) Xia, H.; Kan, R.; Xu, Z.; et al. Two-step tomographic reconstructions of temperature and species concentration in a flame based on laser absorption measurements with a rotation platform. *Opt. Lasers Eng.* **2017**, *90*, 10−18.
(11) Liu, C.; Tsekenis, S.; Polydorides, N.; McCann, H. Toward Customized Spatial Resolution in TDLAS Tomography. *IEEE Sens. J.* **2019**, *19*, 1748−1755.
(12) Liu, C.; Xu, L. Laser absorption spectroscopy for combustion diagnosis in reactive flows: A review. *Appl. Spectrosc. Rev.* **2019**, *54*, 1−44.
(13) Liu, C.; Cao, Z.; Lin, Y.; Xu, L.; McCann, H. Online Cross-Sectional Monitoring of a Swirling Flame Using TDLAS Tomography. *IEEE Trans. Instrum. Meas.* **2018**, *67*, 1338−1348.
(14) Huang, A.; Cao, Z.; Zhao, W.; Zhang, H.; Xu, L. Frequency-Division Multiplexing and Main Peak Scanning WMS Method for TDLAS Tomography in Flame Monitoring. *IEEE Trans. Instrum. Meas.* **2020**, *69*, 9087−9096.
(15) Choi, D.-W.; Doh, D. H.; Jeon, M. G. The development of the simultaneous reconstruction of 2D temperature and concentration using a 6-peaks algorithm for CT-TDLAS. *J. Mech. Sci. Technol.* **2020**, *34*, 2067−2074.
(16) Jeon, M.-G.; Hong, J.-W.; Doh, D.-H.; Deguchi, Y. A study on two-dimensional temperature and concentration distribution of Propane-Air premixed flame using CT-TDLAS. *Mod. Phys. Lett. B* **2020**, *34*, No. 2040020.
(17) Zhang, K.; Sun, M.; Han, T. X.; Yuan, X.; Guo, L.; Liu, T. Residual Networks of Residual Networks: Multilevel Residual Networks. *IEEE Trans. Circuits Syst. Video Technol.* **2018**, *28*, 1303−1314.
(18) Ouchi, S.; Ito, S. Reconstruction of Compressed-sensing MR Imaging Using Deep Residual Learning in the Image Domain. *Magn. Reson. Med. Sci.* **2021**, *20*, 190−203.
(19) Chang, Y.; Yan, L.; Liu, L.; Fang, H.; Zhong, S. Infrared Aerothermal Nonuniform Correction via Deep Multiscale Residual Network. *IEEE Geosci. Remote Sens. Lett.* **2019**, *16*, 1120−1124.
(20) Ronneberger, O.; Fischer, P.; Brox, T. U-Net: Convolutional Networks for Biomedical Image Segmentation *Computer Vision and Pattern Recognition* 2015, DOI: 10.48550/arXiv.1505.04597.
(21) Guan, S.; Khan, A. A.; Sikdar, S.; Chitnis, P. V. Fully Dense UNet for 2-D Sparse Photoacoustic Tomography Artifact Removal. *IEEE J. Biomed. Health Inf.* **2020**, *24*, 568−576.
(22) Zang, H.; Zhu, L.; Ding, Z.; Li, X.; Zhan, S. Cascaded Dense-UNet for Image Super-Resolution. *J. Circuits, Syst. Comput.* **2020**, *29*, No. 2050121.
(23) Jin, J.; Zhang, C.; Feng, F.; Na, W.; Ma, J.; Zhang, Q.-J. Deep Neural Network Technique for High-Dimensional Microwave Modeling and Applications to Parameter Extraction of Microwave Filters. *IEEE Trans. Microwave Theory Tech.* **2019**, *67*, 4140−4155.
(24) Maimaiti, M.; Liu, Y.; Luan, H.; Sun, M. Enriching the transfer learning with pre-trained lexicon embedding for low-resource neural machine translation. *Tsinghua Sci. Technol.* **2022**, *27*, 150−163.
(25) Lei, Shi.; Gangrong, Qu.; Yunsong, Zhao. Ultra-limited-angle CT Image Reconstruction Algorithm Based on Reweighting and Edge-preserving. *J. X-Ray Sci. Techno.* **2021**, 1−13.
(26) Huang, J.; Liu, H.; Dai, J.; Cai, W. Reconstruction for limited-data nonlinear tomographic absorption spectroscopy via deep learning. *J. Quant. Spectrosc. Radiat. Transfer* **2018**, *218*, 187−193.
(27) Xiao, P.; Yin, Y.; Liu, B.; Jiang, B.; Malaiya, Y. K. Adaptive Testing Based on Moment Estimation. *IEEE Trans. Syst., Man, Cybern.: Syst.* **2020**, *50*, 911−922.
(28) Li, X. Image Recovery Via Hybrid Sparse Representations: A Deterministic Annealing Approach. *IEEE J. Sel. Top. Signal Process.* **2011**, *5*, 953−962.
(29) Bing, X.; Xiaojian, H.; Xuanda, L.; Ziqi, H.; Hanchang, Z. Simulation of an NSGA-III Based Fireball Inner-Temperature-Field Reconstructive Method. *IEEE Access* **2020**, *8*, 43908−43919.
(30) Umehara, K.; Ota, J.; Ishida, T. Application of Super-Resolution Convolutional Neural Network for Enhancing Image Resolution in Chest CT. *J. Digital Imaging* **2018**, *31*, 441−450.
(31) Catalbas, M. C. Modified VDSR-based single image super-resolution using naturalness image quality evaluator. *Signal, Image Video Process.* **2022**, *16*, 661−668.
(32) Deng, Z.; He, C.; Liu, Y.; Kim, K. C. Super-resolution reconstruction of turbulent velocity fields using a generative adversarial network-based artificial intelligence framework. *Phys. Fluids* **2019**, *31*, No. 125111.

https://doi.org/10.1021/acsomega.2c01435
ACS Omega 2022, 7, 18722−18731